Alignment and Characterisation of Remote-Refocusing Systems

WENZHI HONG,[1] HUGH SPARKS,[1] AND CHRIS DUNSBY,[1,*]

[1]*Photonics Group, Physics Department, Imperial College London, London, UK*
**christopher.dunsby@imperial.ac.uk*

Abstract: The technique of remote refocusing is used in optical microscopy to provide rapid axial scanning without mechanically perturbing the sample and in techniques such as oblique plane microscopy that build on remote refocusing to image a tilted plane within the sample. The magnification between the pupils of the primary (O1) and secondary (O2) microscope objectives of the remote-refocusing system has been shown previously by Mohanan and Corbett [J Microsc, 288(2):95-105 (2022)] to be crucial in obtaining the broadest possible remote-refocusing range. In this work, we performed an initial alignment of a remote-refocusing system and then studied the effect of axial misalignments of O1 and O2, axial misalignment of the primary tube lens (TL1) relative to the secondary tube lens (TL2), lateral misalignments of TL2 and changes in the focal length of TL2. For each instance of the setup, we measured a Strehl metric, the FHWM of 100 nm fluorescent beads and the axial and lateral distortion of the system: all of these quantities were mapped over the remote-refocusing range and as a function of lateral image position. This allowed us to estimate the volume over which diffraction-limited performance is achieved and how this changes with the alignment of the system.

1. Introduction

The technique of remote refocusing introduced by Botcherby et al. [1] consists of three microscopes in series. The first two microscopes consist of objectives O1 and O2 and tube lenses TL1 and TL2 respectively. These microscopes are arranged in a back-to-back configuration, with the overall magnification set to match the ratio of the refractive indices in the sample and intermediate spaces. This produces an intermediate image with equal lateral and axial magnification. The third microscope then provides a magnified image of a user-defined plane within the intermediate image, which can be refocused away from the focal plane of the first microscope objective. This allows the focal plane of a high numerical aperture objective microscope system to be scanned without mechanically disturbing the sample. Remote refocusing has found numerous applications in high-speed 2D and 3D multiphoton microscopy [2, 3]. It has also been applied in various other imaging techniques, such as spinning disk-remote focusing (SD-RF) microscopy [4], remote-refocusing light-sheet microscopy [5] and oblique plane microscopy (OPM) where remote refocusing is used to generate an image of a tilted plane in the sample [6]. The effectiveness of remote refocusing has been demonstrated in diverse biological systems, including imaging of neural circuits [7], embryonic development [3], and dynamic imaging in isolated cardiomyocytes [5].

Prior research into the performance of remote-refocussing systems has primarily investigated the impact of overall magnification and spherical aberration [8]. However, no analysis of the performance of remote-refocusing systems both on and away from the optical axis and in the presence of misalignments of different optical elements has yet been conducted. In order to better understand how different alignment parameters affect the performance of remote-refocussing systems, a folded test-rig system (O1 = 60x/1.2NA water and O2 = 50x/0.95NA air) employing a star test mask (STM) and 100 nm diameter fluorescent beads as test objects was developed. We demonstrate the effect of different misalignments of O1, O2 and TL2 by analysing the system distortion using the STM and the system resolution through the full width half maximum (FWHM) measurements of 100 nm beads within a refocusing

range from -100 μm to 100 μm. Our findings highlight the critical role of proper alignment in the performance of remote-refocusing systems. The results illustrate the 3D region over which diffraction-limited remote refocussing is achieved both on and away from the optical axis for a specific remote-refocussing system implementation.

2. Methods

2.1 Optical setup

The configurations of the transmitted light and epi-fluorescence imaging modes of the test-rig system are shown in Fig. 1(a) and Fig 1(b) respectively. In the transmitted-light mode, light from a 530 nm LED light source (M530F2, Thorlabs) is directed through an aspheric lens (AL, 350230-B, Thorlabs) with a focal length of 4.5 mm to create a ~20 mm diameter illumination beam on a Lambertian diffuser (LD, 50 DO 50, Comar Optics). The size of the illumination spot on the diffuser is chosen to try and ensure that the illumination NA exceeds that of O1. The alignment object, a star test mask (STM, JD Photo Data), consists of a hexagonal array of 1 μm diameter pinholes in a chrome coating with a spacing of 20 μm. A 0.17 mm (#1.5) thick precision coverslip (630-2186, Marienfield) is placed in contact with the STM, and a drop of water is placed between them. The correction collar for O1 is then set to near the 0.17 mm coverslip position so as to provide symmetrical defocus around the focus position. The LD and STM are placed in contact and mounted on an XYZ translation stage. The XY motion is provided by a manually controlled stage (XY Stage, XYT1/M, Thorlabs) that is mounted on a motorised stage (Stage 1, M-UMR8.25 and TRA25CC, Newport) that provides Z motion to achieve sample refocusing with a minimum actuator step size of 0.2 μm. Following imaging through the objective (O1, 60×, 1.2NA water immersion, MRD07602, Nikon), the beam proceeds through a 4-f system incorporating TL1 (f = 200 mm, ITL200, Thorlabs) and TL2 (composed of D1 (f = 300 mm, 322305000, Linos) and D2 (f = 300 mm, AC508-300-A, Thorlabs)). The separation of D1 and D2 are adjusted as described in the alignment procedure below to achieve a focal length of 162.4 mm. The beam then propagates towards the secondary objective (O2, 50×, 0.95NA air, MPLAPON, Olympus) via a polarising beamsplitter (PBS, 49002, Edmund Optics) and a quarter-wave plate (QWP, AQWP10M-580, Thorlabs) with a 3°53' tilt (using a pair of shim plates, SM1W353, Thorlabs) to avoid unwanted back reflections. A refocusing mirror (M2, PF10-03-G01, Thorlabs) is placed near the focal plane of O2 that is also driven by a motorised stage (Stage 2, M-UMR8.25, TRA25CC, Newport). The reflected beam is finally collected via O2 and TL3 (f = 200 mm, TTL200A, Thorlabs) to a sCMOS camera (C2, ORCA-Fusion, Hamamatsu). M1 in Fig.1 (a) is a detachable mirror (PF10-03-G01, Thorlabs) and is used to direct light from the sample to TL4 (TTL100A, Thorlabs) and a CMOS camera (C1, MQ013CG-E2, Ximea) that is used during positioning of the sample into the focal plane of O1.

For the epi-fluorescence imaging mode (Fig. 1 (b)), a sample of 100 nm diameter fluorescent beads (T7279, TetraSpeck) is used as the imaging object. Epi-fluorescence illumination is achieved by imaging LED2 (M470L2, Thorlabs) to the pupil plane of O1 via a lens pair (L1, LA1401-A and L2 AC508-200-A-ML, both Thorlabs) and a long-pass 495 nm dichroic beamsplitter (DB, 25FF495-Di03, Semrock). An excitation filter (F1, FF01-466/40-25, Semrock) and an emission filter (F2, FF03-525/50-25, Semrock) are placed respectively in front of LED2 and TL3 to prevent excitation light from LED2 reaching camera C2.

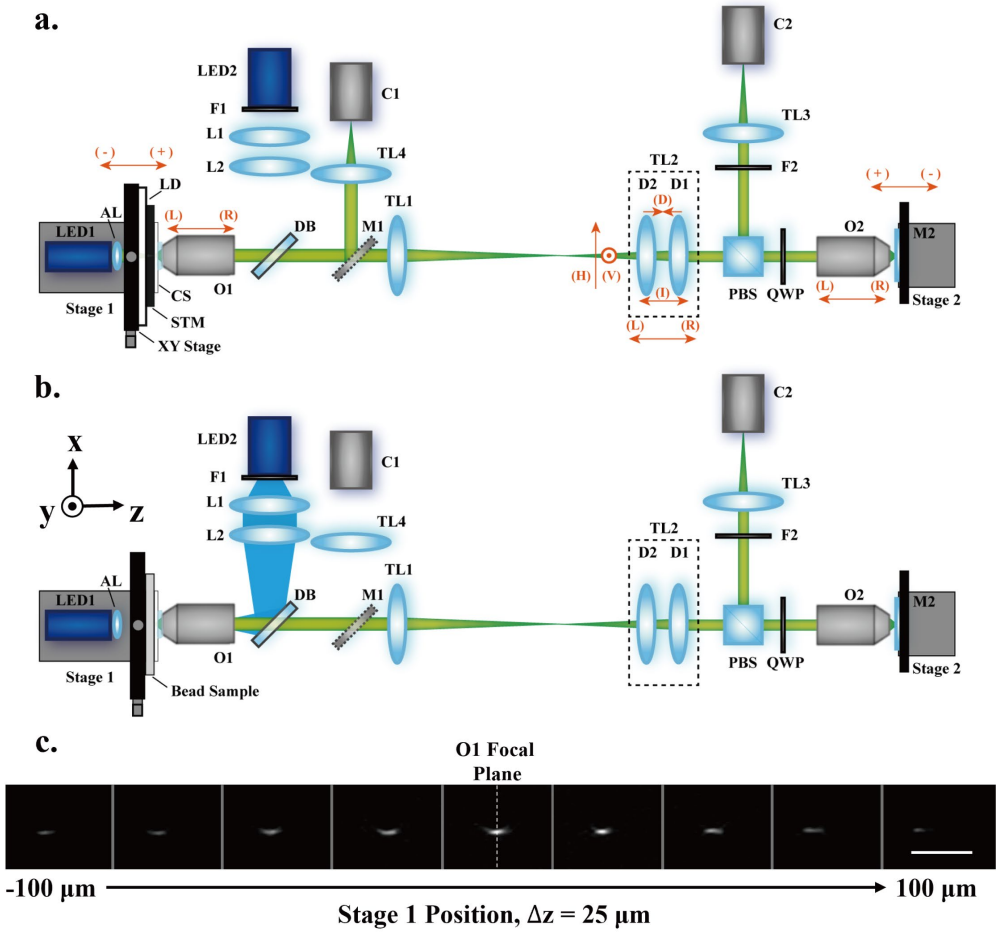

Fig. 1. Configurations of the transmitted light and epi-fluorescence imaging modes of the test rig system. (a) schematic of the transmitted-light mode. (b) schematic of the epi-fluorescence imaging mode. (c) zx-view of sub-regions of interest (sub-ROIs) of the same bead at different Stage 1 positions across the whole refocusing range. Vertical grey lines separate the images taken at different Stage 1 positions. The white dashed vertical line indicates the position of the focal plane of O1. Scale bar, 5 µm. AL, aspheric lens; O, objective; TL, tube lens; M, mirror; L, lens; C, CMOS; D, doublet; F, filter; LD, Lambertian diffuser; STM, star test mask; CS, coverslip; DB, dichroic beamsplitter; PBS, polarising beamsplitter; and QWP, quarter-wave plate. Red arrows in (a) correspond to the stage directions and component misalignment directions.

2.2 Initial System Alignment

Initial alignment of the remote-refocussing setup was performed using the protocol used in our laboratory:

1. The distance between the back focal plane of O1 and the first principal plane of TL1 was set to the focal length of TL1 using a collimated laser diode (PL202, Thorlabs) and shear plate (SI050, Thorlabs).
2. The distance between TL1 and TL2 was set to equal the sum of their focal lengths using the collimated laser diode and shear plate.

3. The initial axial O2 position relative to TL2 was set using the shear plate and collimated laser diode, with the diode incident on the front surface of O2.
4. Then add TL3 and camera C2, with their separation pre-set at the TL3 focal length by imaging an object at infinity.
5. Align the lateral position of TL2 by using STM or USFA test chart as the sample and moving the object to a defocus position of 100 μm with respect to the O1 focal plane. Mark the position of a chosen feature of the object in the C2 image, move the object to the other side of O1 focal plane at -100 μm and refocus the image on C2 using the remote mirror M2 on Stage 2. Adjust the lateral position of TL2 to overlap the object image with the marked position. Five iterations of this process are generally sufficient to remove all measurable lateral motion of the image under changes in refocus.
6. Use the procedure described in section 2.4 to measure the lateral magnification of the system as a function of refocus and the axial magnification of the system.
7. Use the gradient of the lateral magnification to adjust the axial position of O2. In this work, we chose based on experience to define the initial alignment as one where the absolute gradient was less than 5×10^{-5} μm^{-1}. A positive gradient larger than 5×10^{-5} μm^{-1} means that O2 should be moved away from TL2, while a negative gradient smaller than -5×10^{-5} μm^{-1} means that O2 should be moved towards TL2. Return to Step 5. If no adjustment proceed to Step 8.
8. Check whether the system lateral and axial magnifications agree to within 0.01 (This criterion was chosen for the initial alignment based on experience, and considering that for OPM imaging it is important to obtain equal lateral and axial magnifications.) If they do not agree, then adjust the focal length of TL2 and return to Step 5. Once the variation in lateral magnification as a function of refocus (absolute gradient) < 5×10^{-5} μm^{-1}, and lateral and axial magnifications matching to within 0.01 then stop.

Following this procedure the lateral magnification was 1.3322±0.0005 (gradient = $(2\pm0.8)\times10^{-5}$ μm^{-1}) and the axial magnification was 1.334±0.005: this was defined as the initial alignment of the system against which misalignments were compared.

2.3 Control Software and acquisition of system characterisation image data

Translation of the stages and image acquisition were controlled by custom-written LabVIEW software. For each Stage 1 (sample defocus) position, a stack of images is acquired at different Stage 2 (remote refocus) positions. The resulting image data allows for analysis of the characteristics of the remote-refocusing system. When imaging the STM in transmitted light mode, Stage 1 is incrementally moved from -100 μm to 100 μm with 25 μm intervals. At each Stage 1 position, Stage 2 is repositioned to the nominal refocusing plane and scanned from 3 μm to -3 μm around this position with -0.5 μm steps (117 images in total). When imaging the fluorescent beads in epi-fluorescence imaging mode, Stage 2 is scanned over the same range of 3 μm to -3 μm but with the minimum incremental motion of the motorised actuator (-0.2 μm), resulting in 279 images. Exemplar zx sub-ROIs for one bead are shown in Fig. 1 (c). The plus and minus signs of the stage directions are indicated in Fig. 1 (a).

2.4 Characterisation of lateral and axial magnification

The system lateral and axial magnifications were determined from images of the star test mask in transmitted light mode with 0.5 μm steps of Stage 2. For each Stage 1 (sample defocus) position, a square ROI with side 60 pixels was defined for each pinhole within the centre 67×67 μm^2 of the field of view (FOV) and used to find the maximum pixel value of each pinhole. The image with the highest average maximum pinhole pixel value was then selected as the in-focus image, which corresponds to the Stage 2 position closest to where the STM is in focus on C2.

The central location of each pinhole in each in-focus image was determined by first subtracting a background, which was estimated by morphologically opening the raw image with a disk structuring element (radius of 15 pixel), and then applying a threshold (twice the

average of the estimated background) to the image for binarisation [9]. Pinhole regions were then found by finding connected components in the binary image. The position of each pinhole was then determined from the centroid of its image within each connected component. The average of adjacent pinhole separations within the centre of FOV (67×67 μm^2) where the lateral distortion is relatively small and stable (see Fig.2 (d)), was calculated to estimate the lateral magnification for each Stage 1 (sample defocus) position. This process was repeated for all 9 Stage 1 (sample defocus) positions over the range from -100 μm to 100 μm and the lateral magnification was plotted as a function of Stage 1 position, see Fig. S1 (a) for an example measured using the initial alignment of the system. A linear function was then fit to the data to determine the gradient and y-intercept using MATLABs *fitlm* function, which returns standard deviations on the fit parameters. The y-intercept obtained from this plot was used as the system lateral magnification.

To determine the axial magnification, two times the Stage 2 positions from the 9 in-focus images were plotted as a function of Stage 1 (sample defocus) position. (The Stage 2 position is doubled to give the optical path length change on reflection.) A linear fit is applied to the data, again using MATLABs *fitlm* function, and the gradient provides the negative of the axial magnification (see Fig. S1 (b) for an example of the initial system).

The random error on the measurement of the lateral magnification, axial magnification, and gradient of lateral magnification with refocus distance was taken to be the average standard deviations from the *fitlm* fitting function over all measurements presented in this work. This yielded an error of 0.0005 for the lateral magnification, 0.005 for the axial magnification and 8×10^{-6} for the gradient of the lateral magnification as a function of sample refocus distance.

The spacing of the pinholes in the STM were checked using a transmitted light microscope frame fitted with a motorized x-y stage with a linear encoder. A pinhole spacing of 20.00±0.02 μm was determined, which leads to a maximum estimated systematic error on the lateral magnification of 0.0014.

2.5 Characterisation of System Distortion

As the 1 μm diameter pinholes in the STM are arranged in a hexagonal array, it is possible to estimate the lateral distortion introduced by the refocusing system by calculating the distance between each pinhole in an in-focus image of the STM (mentioned in section 2.4) to the nearest pinhole in a predetermined reference pinhole hexagonal array. The pinhole closest to the FOV centre in the in-focus image at 0 μm sample defocus position was selected as the centre predetermined reference pinhole. The system lateral magnification measured in section 2.4 was then used to generate the predetermined reference pinhole hexagonal array. The 9 in-focus images at different Stage 1 positions were analysed to calculate the lateral distortion. These values were then utilised to generate a lateral distortion map as a function of the distance from the FOV centre (see Fig. 2 (d)).

To measure the axial distortion, the 7 images with the highest average maximum pixel value of pinholes within the FOV centre were selected at each Stage 1 (sample defocus) position. For each Stage 1 (sample defocus) position, the intermediate image defocus was determined by subtracting the nominal Stage 2 position obtained from the refractive index of water from the corresponding Stage 2 position of the in-focus image. Field curvature maps were obtained by considering each individual pinhole. The axial distortion for a pinhole was determined by the displacement between the nominal Stage 2 position and the position that produced the highest Strehl ratio for the pinhole, see also [10, 11]. To account for the double-pass effect of M2 and the nominal axial magnification of the system, the displacements were converted into axial distortion in sample space by multiplying a factor of 2/1.333 = 1.5. An axial distortion map for 9 sample defocus positions was then generated as a function of the distance to the FOV centre (see Fig. 2 (e)).

2.6 System Characterisation of Resolution

To characterise the system resolution, epi-fluorescence images of the 100 nm fluorescent bead sample were acquired with the finer Stage 2 step size of 0.2 μm. By considering the NA of the system of 1.2 (limited by O1), an emission wavelength of 525 nm, the 100 nm bead diameter, the 6.5 μm pixel size and the lateral magnification of 74.0×, a theoretical lateral resolution with full width at half maximum (FWHM) of 0.26 μm was estimated by assuming these factors can be approximated by independent Gaussian distributions of equivalent FWHMs. For each Stage 1 (sample defocus) position, 31 images were acquired corresponding to an interval of 0.3 μm in sample space (see example data from one bead shown in Fig. 1 (c)). At each sample defocus position, a difference of Gaussians (DoG) filter (sigma values of 1.0 and 1.46 pixels) [12] was applied and followed by a binarisation step and identification of connected components. The threshold was chosen by gradually increasing the threshold until the number of detected components reached a steady value. The 3-dimensional coordinates (x, y, z) of each bead were then found from the location of the pixel with maximum value within each connected component mask. A preliminary analysis was conducted first to find the average peak bead intensity. To reject bead clusters or hot pixels, the formal analysis was then carried out using an intensity filter that only selects beads with peak intensity ranging from two thirds to four thirds of the average peak intensity. Two orthogonal 1D-Gaussian fits in the lateral (x, y) directions of each bead were applied within a sampling box with sides 1.58 μm in sample space, and utilised to calculate a mean lateral FWHM value of the bead image.

As another metric for system performance, we also calculated a Strehl metric for each bead. To do this, the normalised maximum pixel value of each bead was calculated by first subtracting off the average offset determined during the two 1D-Gaussian fits. The maximum pixel value of each bead was then divided by the sum of all pixel values within a circle with a diameter of 20 pixels (7-fold of the theoretical bead FWHM). The Strehl ratio of each bead was then calculated by dividing the normalised maximum pixel value by the ideal normalised maximum pixel value of a 100 nm bead. The ideal normalised maximum pixel value was calculated by convolving the theoretical Airy PSF with a disk with the same radius as the fluorescent bead and then binning the data with the known camera pixel size [10, 11]. The mean lateral FWHM ($FWHM_{xy}$) and Strehl ratio of beads were respectively analysed to produce a 2D histogram (displayed as a heatmap) with contours (see Fig. 2 (a-b)). The diffraction-limited volume (see Table S3) was then obtained by finding the volume encompassed by the bins of the 2D histogram with mean Strehl ratio ≥ 0.8 in the mean Strehl ratio map (Fig. 2 (a)). A normalised peak bead intensity map (Fig. 2 (c)) was also generated by recording the peak intensity of each bead that passed through the intensity filter. All three maps were plotted as functions of sample defocus and bead distance to the FOV centre.

2.7 Sample preparation

100 nm fluorescence beads (T7279, TetraSpeck) were diluted 500-fold and attached to a precision #1.5 coverslip (630-2186, Marienfield) with poly-L-lysine (100 μL diluted in 10 μL water, P8920, Sigma-Aldrich). The coverslip then was mounted on a glass slide (12392098, Epredia) with mounting media polyvinyl acetate (PVA, 475904 Millipore, Mowiol) and sealed with silicone sealant (ZA22, Polycraft).

3. Results

3.1 Axial Misalignments of O1 and O2

To investigate the impact of O1 and O2 axial misalignments on remote-refocusing systems, the O1 position in the initial setup was shifted by 1 mm towards TL1 (denoted as (R) in Fig. 1(a) and Fig. 2), as well as 1 mm away from TL1 (denoted as (L) in Fig. 1(a) and Fig. 2). O1 was returned to its initial position and then O2 was adjusted from its position in the initial setup by 2 mm towards TL2 (denoted as (L) in Fig. 1(a) and Fig. 2), as well as 2 mm closer to M2

(denoted as (R) in Fig. 1(a) and Fig. 2). The STM and 100 nm bead samples were imaged under these four misalignments to characterise the system distortion and resolution (see Fig. 2 and Fig. S2).

The plots of lateral magnification measured for different O1 axial position are shown in Fig. S2 (p). Moving O1 towards TL1 (R) causes the pupil of O1 to be imaged to the right of the pupil of O2. Therefore, axially misaligning O1 away from its position in the initial setup causes the gradient of the lateral magnification as a function of sample defocus to decrease and become negative when moved to the left (L) and increase when moved to the right (R) as expected, see also Table S2. Axially misaligning O2 has a similar effect to O1 axial misalignment but the direction of the change in gradient with respect to direction of movement of O2 is reversed, see Fig. 2 (p), again as expected.

The intermediate image defocus as a function of sample defocus are shown in Fig. 2 (q) and Fig. S2 (q) and were fitted to second-order polynomials. The magnitude of the quadratic term increases compared to the initial condition when O2 was adjusted by 2 mm away from TL2 (R) and decreases and becomes negative when O2 was adjusted by 2 mm towards TL2 (L), see Fig. 2 (q). A similar effect occurs in Fig. S2 (q) when O1 was shifted 1 mm closer to TL1 (R), the magnitude of the quadratic term for this misalignment is lower than that of the initial system. The axial misalignment of O2 in the two directions has approximately equal and opposite effects on lateral and axial distortion (compare Fig. 2 (i, n and j, o)) and on average increases system lateral distortion, see Table S3. Average axial distortion is increased for motion to the right (R) and marginally decreased for motion to the left (L). As the axial misalignment of O1 is smaller (1 mm compared to 2 mm for O2), the effect on distortion is more subtle. Motion of O1 to the left (L) results in a similar effect to the motion of O2 to the right (R), see Fig. S2 (n-o). The average distortion for motion of O1 to the right (R) decreases the average lateral and axial distortion (Table S3).

In terms of the resolution characterisation, the axial misalignments of O1 and O2 reduce the diffraction-limited volume by more than 43% (see Table S3), which can also be seen by the smaller region over which a mean Strehl ratio of 0.8 is achieved, see Fig. 2 (a,f,k) and Fig. S2 (a,f,k) and the region over which a PSF FWHM of 0.26 μm is achieved, see Fig. 2 (b,g,l) and Fig. S2 (b,g,l). The normalised peak bead intensity distribution as a function of sample defocus also becomes narrower Fig. 2 (c,h,m) and Fig. S2 (c,h,m).

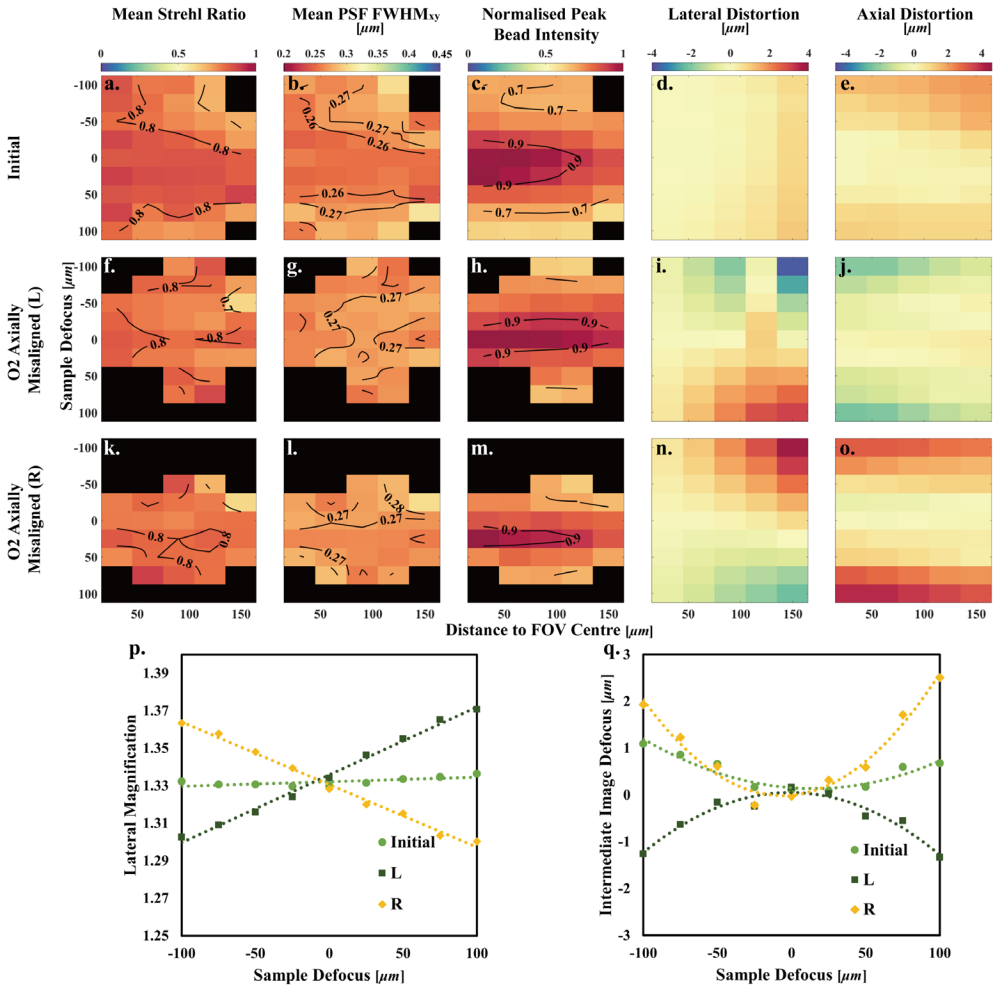

Fig. 2. Characterisation of O2 axial misalignment. (a-e) Initial system. (f-j) O2 axially misaligned by 2 mm towards TL2. (k-o) O2 axially misaligned by 2 mm towards M2. Black blocks indicate no bead recognised in those regions. (p) Lateral magnification as a function of sample defocus. The dashed lines are the linear fits to the measured data points. (q) Intermediate image defocus as a function of sample defocus. The dashed curves are the second-order polynomial fits to the measured data points.

3.2 Axial and Lateral Misalignments of TL2

As stated in section 2.2, the axial distance between TL1 and TL2 was aligned via a shear plate so they are separated by the sum of their focal lengths. Shear plate alignment error was estimated to be 1.54 mm via the standard deviation of ten measurements of TL1 with respect to TL2 in the test rig system. Therefore, the axial misalignments of TL2 were conducted by positioning TL2 2 mm (larger than the shear plate alignment error) to the left and right from the initial position. In both TL2 axial misalignments, O2 was also realigned to reduce the variation in lateral magnification with defocus to less than 5×10^{-5} μm^{-1}, as per the initial alignment procedure (see Fig. 3 (p) and Table S2). The results of the characterisation are shown in Fig. 3. The mean Strehl ratio map in Fig. 3 (k) is slightly better than the initial system (larger diffraction-limited volume, increased by 7%, see Table S3), but the sample defocus range over which the bead intensity is maintained is slightly narrower (see Fig. 3(m)). Under TL2 axial misalignments in both directions, the mean absolute lateral distortion decreases from the initial

alignment, while the mean absolute axial distortion decreases for one direction (L) and increases for the other (R) see Fig. 3 (d-e, i-j and n-o) and Table S3.

Lateral misalignments of TL2 were achieved by adjusting the cage system translating lens mount (CXY2, Thorlabs) horizontally and vertically by 0.5 turns of the relevant micrometer (~0.13 mm) from the initial system. The characterisation of TL2 lateral misalignment (see Fig. S3) shows that although the lateral and axial distortions only change slightly from the initial system (see Table S3, mean distortion absolute difference from the initial system < 0.3 μm), laterally misaligning TL2 causes a decrease in the FOV over which a good image quality is achieved (> 80% reduction in the diffraction-limited volume, see Table S3). Hence, TL2 lateral alignment is an essential part in the remote-refocusing alignment procedure.

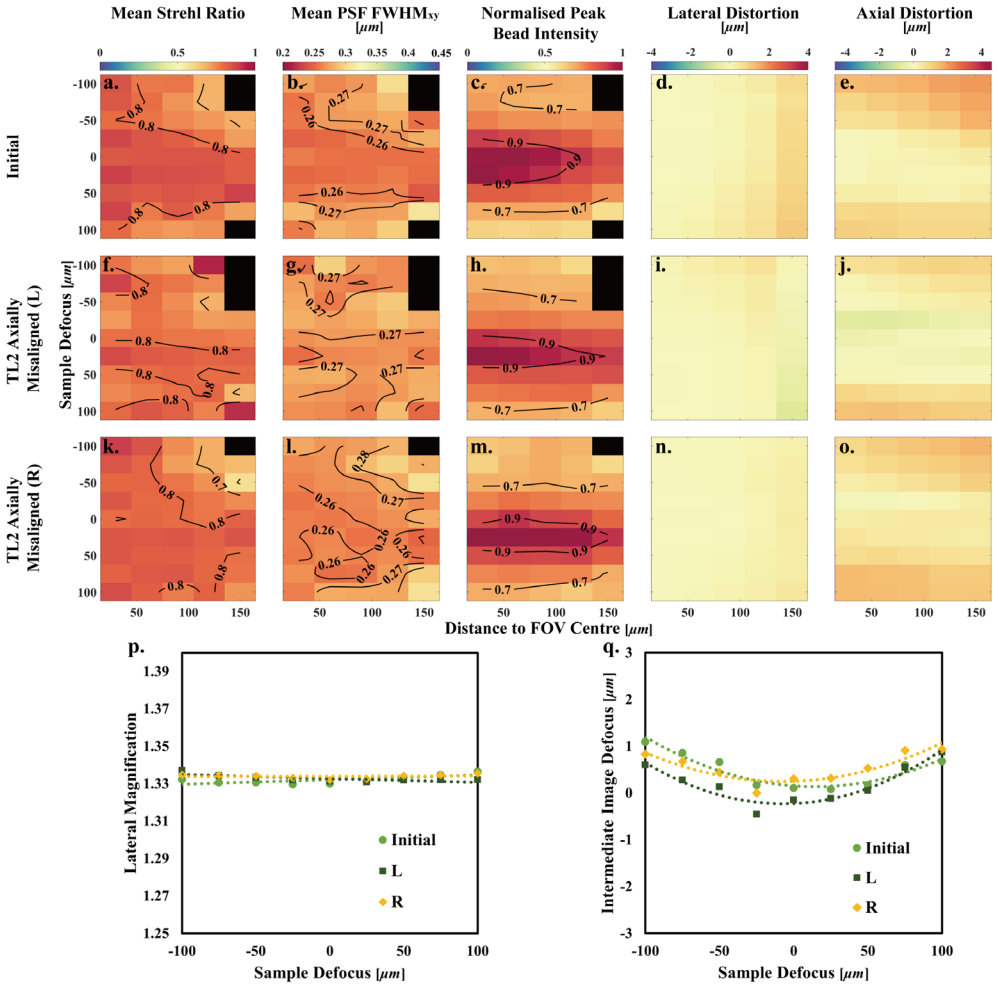

Fig. 3. Characterisation of TL2 axial misalignment. (a-e) Initial system. (f-j) TL2 axially misaligned by 2 mm towards TL1. (k-o) TL2 axially misaligned by 2 mm towards O2. (p) Lateral magnification as a function of sample defocus. The dashed lines are the linear fit lines to the measured data points. (q) Intermediate image defocus as a function of sample defocus. The dashed curves are the second-order polynomial fits to the measured data points.

3.3 Misalignment of TL2 focal length

In remote-refocusing systems, given the commercial tube lenses only provide specific focal lengths, TL2 can be formed by two achromatic doublets with an adjustable separation [13]. Different TL2 focal lengths were also tested to analyse the effect of overall magnification

mismatch in remote-refocusing systems. The TL2 focal length was slightly increased (I) by increasing the separation of D1 and D2 (compared to initial alignment of TL2) by 2 turns of Thorlabs SM2 tube with pitch of 40 turns per inch, which is approximately 1.27 mm. The TL2 focal length was also decreased (D, 4 turns of SM2 tube from the initial TL2, which is approximately 2.54 mm), see Fig. 1. In both cases, the axial position of TL2 was then aligned relative to TL1 via the shear plate, and O2 was also adjusted to bring the variation in lateral magnification with defocus to less than 5×10^{-5} μm^{-1}, as per the initial alignment procedure.

The measured lateral and axial magnifications of these two misaligned systems are in Table S1. When the focal length was increased compared to the initial system (I), the system lateral magnification decreased slightly from 1.3322 to 1.3321 as expected, although well within the measurement random error of 0.0005, leading to a broader diffraction-limited region as depicted in the mean Strehl ratio map and a larger diffraction-limited volume, increased by 24% (see Fig. 4 (f) and Table S3). Smaller lateral and axial distortions were also observed in Fig. 4 (i-j) and Table S3. Conversely, an increase in the system lateral magnification from 1.3322 to 1.3375 resulted in a decrease in the diffraction-limited region in the mean Strehl ratio map (see Fig. 4 (k)) and a smaller diffraction-limited volume, decreased by 65% (see Table S3). Altering the focal length of TL2 also resulted in a modification of the system axial distortion, as depicted in Fig. 4 (j,o,q).

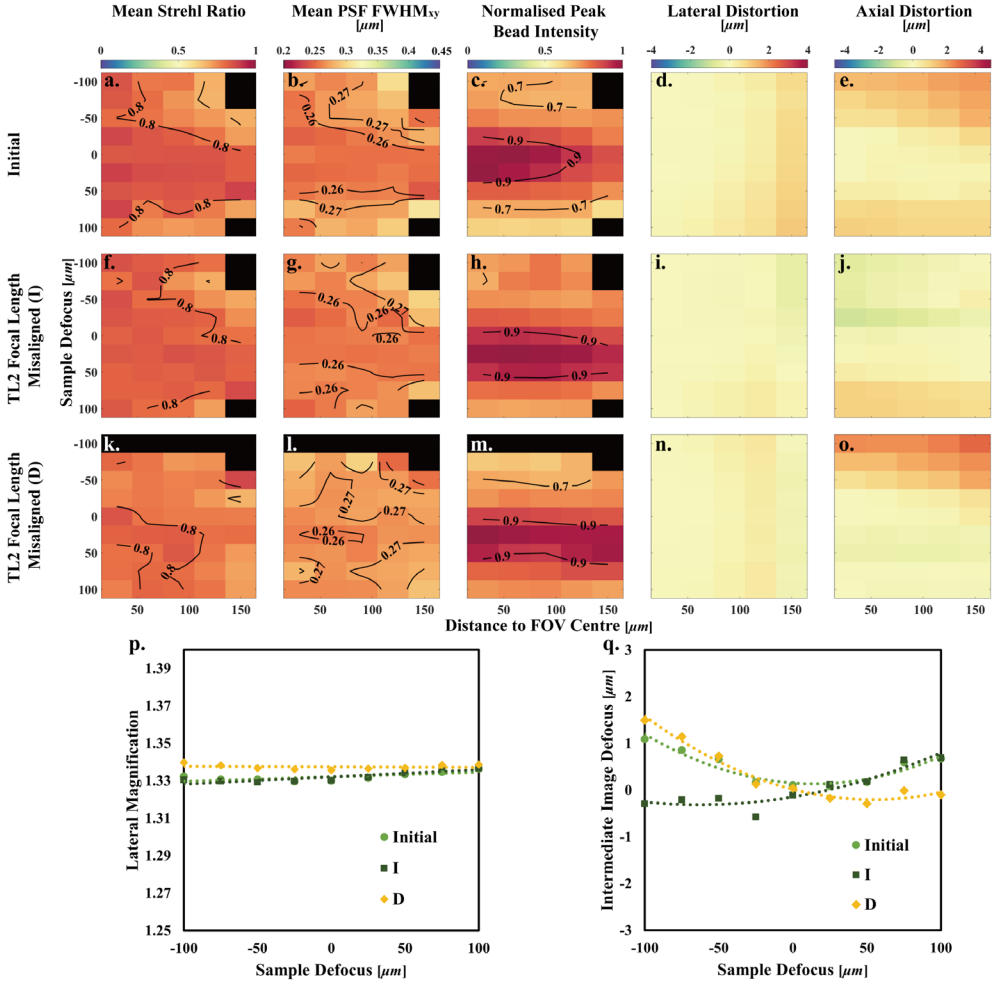

Fig. 4. Characterisation of TL2 focal length misalignment. (a-e) Initial system. (f-j) TL2 with increased focal length. (k-o) TL2 with decreased focal length. (p) Lateral magnification as a function of sample defocus. The dashed lines are the linear fitting lines to the measured data points. (q) Intermediate image defocus as a function of sample defocus. The dashed curves are the second-order polynomial fits to the measured data points.

4. Discussion

According to the results presented above, axial misalignments of O1 (±1 mm) and O2 (±2 mm) have a similar effect on the remote-refocusing system studied here and cause the lateral magnification to vary across the refocusing range. It also causes a reduction (≥ 43%) in the 3D region over which initial diffraction-limited imaging is achieved. In fig. S2 (q), movement of O1 to the right by 1 mm (R) caused a decrease in the quadratic dependence of the intermediate image defocus as a function of sample defocus compared to the initial condition. When comparing to fig. 2 (q), it seems likely that this misalignment introduces a negative axial distortion that partially compensates for the expected axial distortion in the overall system [14], however this comes at the cost of the reduction in diffraction-limited image volume mentioned above.

Axial misalignment of TL2 to the left (L) by -2 mm relative to TL1 caused a reduction (40%) in diffraction-limited volume. Misalignment to the right caused a small increase in diffraction-limited volume (7%), a decrease in mean lateral distortion but a slight increase in mean axial distortion (Table S3) that was accompanied by an increase in the lateral magnification to 1.3340 compared to the initial alignment of 1.3322. This change in lateral magnification is greater than the random error on the lateral magnification of 0.0005 and we estimate that the change in diffraction-limited volume is on the same order as the error on the measurement.

In comparison, lateral misalignment (±0.13 mm) of TL2 resulted in an average reduction of the diffraction-limited FOV by 85%. We suggest that lateral alignment of TL2 is required after any adjustment of other optical elements.

Increasing (I) the focal length of TL2 resulted in a decrease of mean lateral distortion, a decrease in mean axial distortion and an increase of 24% in the diffraction-limited volume. Therefore, this alignment provides better performance compared to the initial alignment. This change caused a decrease in the lateral magnification from the initial value of 1.3322 to 1.3321, which is smaller than the random error on the lateral magnification (0.0005).

The importance of achieving the correct magnification between the pupils of O1 and O2 has already been demonstrated by Mohanan and Corbett [8], who showed that a 1% magnification mismatch leads to a 50% reduction in the remote-refocusing range.

In this work, we have considered the lateral extent of the diffraction-limited region as well as its axial extent. This has allowed us to estimate the volume over which diffraction-limited performance is achieved and show it to be sensitive to the alignment of a number of the optical components.

The ideal lateral of the magnification of the refocusing system should theoretically be equal to the ratio of refractive indices between the sample and remote spaces. For the system here, this should be equal to the refractive index of water, which is given for 20°C and 1 bar as 1.33626 at 515 nm, and 1.33348 at 589 nm [15]. All experiments performed here were carried out using wavelengths over the range 500-550 nm. Linear interpolation of the tabulated values gives a refractive index for water of 1.3359 at the centre wavelength used here of 525 nm.

As pointed out by theoretical calculations by Mohanan and Corbett, see figure 6 of [8], small variations in the lateral magnification on the order of 0.995-1.005 can lead to defocus as a function of refocus distance (axial distortion) that partially compensates for spherical aberrations and increases the diffraction-limited refocus range when considering points along optical axis. These variations in lateral magnification are expected to lead to a shift in where the best imaging performance is obtained to one side of the focal plane of O1.

The lateral magnification of the initial alignment of our system (1.3322) varies from the refractive index of water (1.3359 at 525 nm) by more than the estimated systematic error on

our lateral magnification (0.0014). However, the variation of axial distortion as a function of sample defocus is reasonably symmetrical about zero sample defocus, see Fig. 4 (e&q), suggesting a good mapping of the pupil of O1 to the pupil of O2. When increasing the focal length of TL2 (I), we see the position of minimum axial distortion shift to the left in Fig. 4(q), and when decreasing the focal length of TL2 (D) we see a shift to the right. This is broadly consistent with what is expected based on Fig. 6 of [8] as small amounts of defocus (distortion) compensate for spherical aberration.

5. Conclusion

This paper presents an analysis of the effects of misalignment on a remote-refocusing system employing a 60×/1.2NA water Nikon O1 lens and a 50×/0.95NA air Olympus O2 lens. TL1 was the ITL200 from Thorlabs and TL2 was formed from a pair of achromatic doublets (322305000, Linos and AC508-300-A, Thorlabs). We performed an initial alignment of the system and then studied the effect of axial misalignments of O1 and O2, axial misalignment of TL1 relative to TL2, lateral misalignments of TL2 and axial misalignment of the separation of the two doublets forming TL2 causing a change in the focal length of TL2. For each instance of the setup, we measured a Strehl metric, the FHWM of 100 nm fluorescent beads and the axial and lateral distortion of the system: all of these quantities were mapped over the remote-refocusing range and as a function of lateral image position.

We found that axial movement of O1 by ±1 mm or O2 by ±2 mm caused a reduction in the diffraction-limited imaging volume in the range 43 to 67%. Axial misalignments of TL1 relative to TL2 by ±2 mm on average caused less of a change (-40 and 7%). This motion is slightly larger than the measured alignment error of TL1 and TL2 using a collimated laser diode and shear plate of 1.54 mm and therefore we believe that alignment using this method is a reasonable approach. Lateral motion of TL2 by ~0.13 mm caused the biggest reduction diffraction-limited imaging volume in the range 80 to 90%.

The best performance of our system was achieved when the focal length of TL2 was slightly increased (I) relative to our initial alignment and this gave an estimated diffraction-limited imaging volume of 8.1×10^6 μm^3.

Overall, in order to replicate the alignment achieved using this specific combination of optics, we would suggest that the alignment procedure given in section 2.2 is followed up to step 7, but that step 8 is replaced with a check to see whether the lateral magnification has reached 1.3321 and the variation in lateral magnification as a function of refocus (absolute gradient) $< 5\times10^{-5}$ μm^{-1}.

This paper provides a characterization of the errors due to misalignment for one particular remote-refocusing system. Further work is still required to check if these findings are generally seen in systems employing different optical elements. Further work is also required to find a general procedure that allows for the best alignment to be reached without exploring a range of system lateral magnifications in a small range around that expected.

Funding

The authors gratefully acknowledge funding from UK Engineering and Physical Sciences Research Council grants EP/T003103/1 and EP/R511547/1, and a CRUK Accelerator award (A29368).

Acknowledgements

The authors gratefully acknowledge the expert help from Martin Kehoe and Simon Johnson in the Optics Workshop of the Photonics Group of Imperial College London who helped fabricate the custom components for this remote-refocusing test rig system; Terry Wright for providing his STM pinhole finding and lateral magnification algorithm for our adaptation; Liuba Dvinskikh for valuable advice and discussions on the bead psf fitting procedure; Edwin Garcia Castano for valuable assistance with the bead sample preparation.

Disclosures

CD has filed a patent application on dual-view oblique plane microscopy and has a licensed granted patent on oblique plane microscopy, which both utilise remote-refocusing systems.

References

1. Botcherby EJ, Juskaitis R, Booth MJ, Wilson T. Aberration-free optical refocusing in high numerical aperture microscopy. Optics Letters. 2007;32(14).
2. Hoover EE, Young MD, Chandler EV, Luo A, Field JJ, Sheetz KE, et al. Remote focusing for programmable multi-layer differential multiphoton microscopy. Biomedical optics express. 2011;2(1):113-22.
3. Botcherby EJ, Smith CW, Kohl MM, Debarre D, Booth MJ, Juskaitis R, et al. Aberration-free three-dimensional multiphoton imaging of neuronal activity at kHz rates. Proc Natl Acad Sci U S A. 2012;109(8):2919-24.
4. Gintoli M, Mohanan S, Salter P, Williams E, Beard JD, Jekely G, et al. Spinning disk-remote focusing microscopy. Biomedical Optics Express. 2020;11(6):2874-88.
5. Sparks H, Dvinskikh L, Firth JM, Francis AJ, Harding SE, Paterson C, et al. Development a flexible light-sheet fluorescence microscope for high-speed 3D imaging of calcium dynamics and 3D imaging of cellular microstructure. Journal of Biophotonics. 2020;13(6):e201960239.
6. Dunsby C. Optically sectioned imaging by oblique plane microscopy. Optics express. 2008;16(25):20306-16.
7. Schuetzenberger A, Borst A. Seeing Natural Images through the Eye of a Fly with Remote Focusing Two-Photon Microscopy. iScience. 2020;23(6):101170.
8. Mohanan S, Corbett AD. Sensitivity of remote focusing microscopes to magnification mismatch. J Microsc. 2022;288(2):95-105.
9. Bengtsson A, Bengtsson H. Microarray image analysis: background estimation using quantile and morphological filters. BMC Bioinformatics. 2006;7:96.
10. Hong W, Wright T, Sparks H, Dvinskikh L, MacLeod K, Paterson C, et al. Adaptive light-sheet fluorescence microscopy with a deformable mirror for video-rate volumetric imaging. Applied Physics Letters. 2022;121(19):193703.
11. Wright T, Sparks H, Paterson C, Dunsby C. Video-rate remote refocusing through continuous oscillation of a membrane deformable mirror. Journal of Physics: Photonics. 2021;3(4):045004.
12. Pitas I. Digital image processing algorithms and applications: John Wiley & Sons; 2000.
13. Hong W, Dunsby C. Automatic tube lens design from stock optics for microscope remote-refocusing systems. Optics Express. 2022;30(3):4274-87.
14. Botcherby EJ, Juškaitis R, Booth MJ, Wilson T. An optical technique for remote focusing in microscopy. Optics Communications. 2008;281(4):880-7.
15. Harvey AH, Gallagher JS, Sengers JL. Revised formulation for the refractive index of water and steam as a function of wavelength, temperature and density. Journal of Physical and Chemical Reference Data. 1998;27(4):761-74.

Supplementary Material

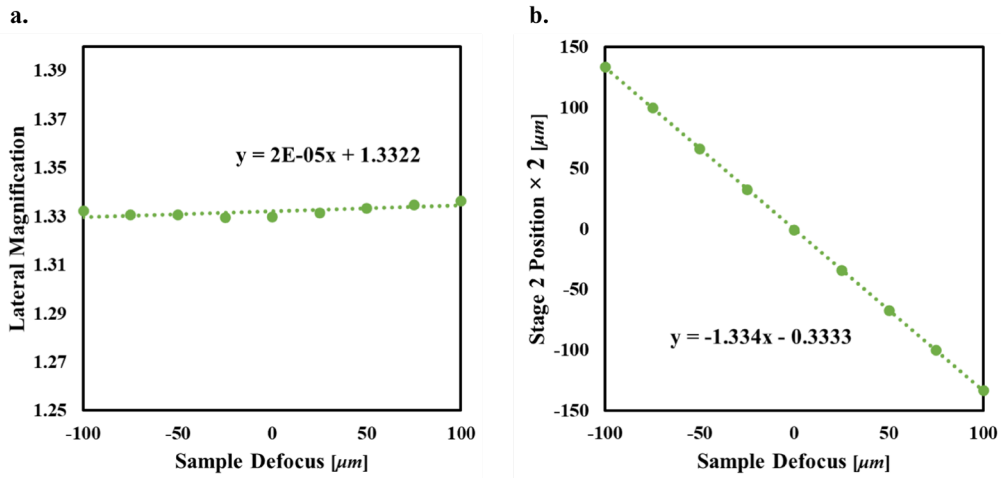

Fig. S1. (a) Linear fit to the measured lateral magnifications within the whole refocusing range. (b) Linear fit to twice the Stage 2 position for the in-focus image as a function of sample defocus. The axial magnification equals to (-) gradient. At each sample defocus, the lateral and axial magnifications were measured from the Stage 2 position closest to the sample being in focus on C2.

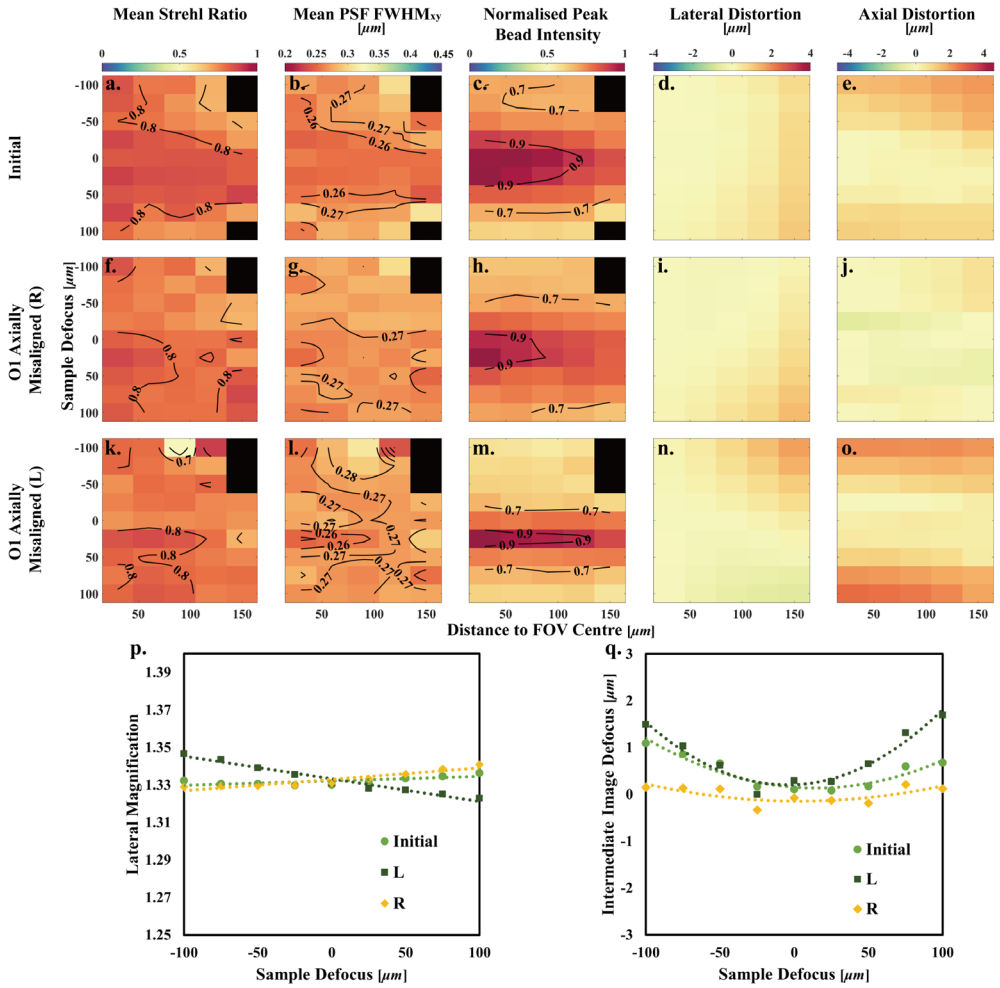

Fig. S2. Characterisation of O1 axial misalignment. (a-e) Initial system. (f-j) O1 axially misaligned by 1 mm towards TL1. (k-o) O1 axially misaligned by 1 mm towards Stage 1. (p) Lateral magnification as a function of sample defocus. The dashed lines are linear fits to the measured data points. (q) Intermediate image defocus as a function of sample defocus. The dashed curves are the second-order polynomial fits to the measured data points.

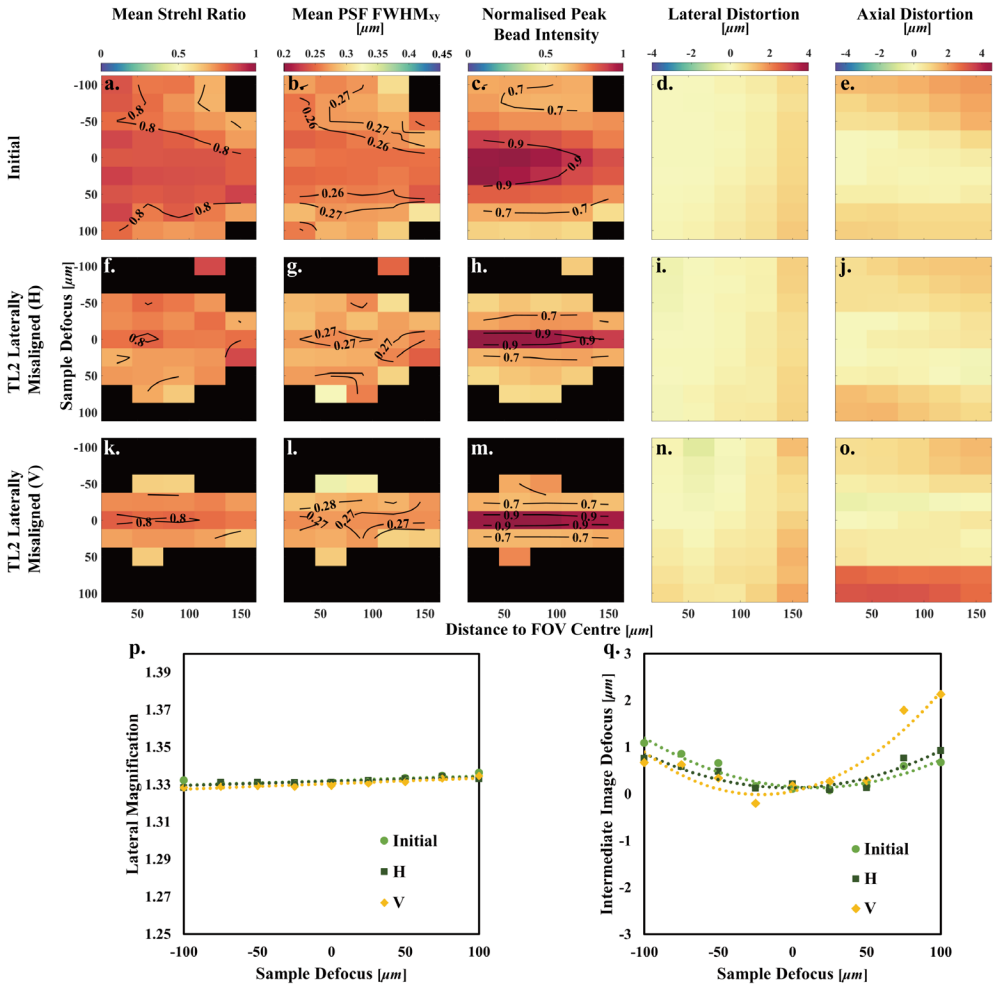

Fig. S3. Characterisation of TL2 lateral misalignment. (a-e) Initial system. (f-j) TL2 laterally misaligned in horizontal direction. (k-o) TL2 axially misaligned in vertical direction. (p) Lateral magnification as a function of sample defocus. The dashed lines are the linear fitting lines to the measured data points. (q) Intermediate image defocus as a function of sample defocus. The dashed curves are the second-order polynomial fits to the measured data points.

Table S1. Lateral and axial magnifications in all tested cases.

Case	Lateral Magnification (FOV centre)	Axial Magnification	Abs (Lateral Magnification - Axial Magnification) *
Estimated random error	±0.0005	±0.005	±0.005
Estimated systematic error	±0.0014		
Initial	1.3322	1.334	0.0018
O1 (R)	1.3330	1.329	0.0037
O1 (L)	1.3332	1.325	0.0085
O2 (L)	1.3358	1.329	0.0065
O2 (R)	1.3306	1.324	0.0066
TL2 (L)	1.3328	1.325	0.0081
TL2 (R)	1.3340	1.325	0.0093
TL2 (H)	1.3318	1.327	0.0051
TL2 (V)	1.3305	1.315	0.0158
TL2 (I)	1.3321	1.315	0.0174
TL2 (D)	1.3375	1.343	0.0058

*: Absolute value.

Table S2. Gradients of measured lateral magnification lines in all tested cases.

Case	Gradient of Lateral Magnification Line (μm^{-1}) $\pm 8\times10^{-6}$
Initial	2×10^{-5}
O1 (R)	6×10^{-5}
O1 (L)	-1×10^{-4}
O2 (L)	4×10^{-4}
O2 (R)	-3×10^{-4}
TL2 (L)	-2×10^{-5}
TL2 (R)	1×10^{-6}
TL2 (H)	2×10^{-5}
TL2 (V)	3×10^{-5}
TL2 (I)	4×10^{-5}
TL2 (D)	-2×10^{-6}

Table S3. Mean absolute lateral and axial distortions and diffraction-limited volume in all tested cases.

Case	Mean absolute lateral distortion* (μm)	Mean absolute axial distortion** (μm)	Diffraction-limited volume ($\times 10^6$ μm^3)	Percentage difference in diffraction-limited volume from Initial*** (%)
Initial	0.31	0.80	6.5	0
O1 (R)	0.28	0.24	3.7	-43
O1 (L)	0.38	1.21	2.4	-63
O2 (L)	1.04	0.77	3.7	-43
O2 (R)	1.01	1.49	2.1	-67
TL2 (L)	0.17	0.54	4.0	-40
TL2 (R)	0.13	0.85	7.0	7
TL2 (H)	0.30	0.68	1.3	-80
TL2 (V)	0.49	1.09	0.6	-90
TL2 (I)	0.13	0.47	8.1	24
TL2 (D)	0.17	0.74	2.3	-65

*: Average over 2D histograms shown in panels d,i,n of figures 2, 3, 4, S2 and S3.
**: Average over 2D histograms shown in panels e,j,o of figures 2, 3, 4, S2 and S3.
***: Percentage Difference from Initial = (Diffraction-limited volume - Diffraction-limited volume of Initial)/ (Diffraction-limited volume of Initial)×100.